Chinese Chemical Letters 34 (2023) 108046

Contents lists available at ScienceDirect

Chinese Chemical Letters

journal homepage: www.elsevier.com/locate/cclet

Dopant-vacancy activated tetragonal transition metal selenide for hydrogen evolution electrocatalysis

Qiuyan Huang[a], Xin Liu[a], Ze Zhang[a], Lianli Wang[b], Beibei Xiao[a,*], Zhimin Ao[c,*]

[a] School of Energy and Power Engineering, Jiangsu University of Science and Technology, Zhenjiang 212003, China
[b] School of Materials Science and Engineering, Xi'an University of Science and Technology, Xi'an 710054, China
[c] Advanced Interdisciplinary Institute of Environment and Ecology, Beijing Normal University, Zhuhai 519087, China

ARTICLE INFO

Article history:
Received 8 September 2022
Revised 2 December 2022
Accepted 5 December 2022
Available online 7 December 2022

Keywords:
Hydrogen evolution reaction
Transition metal selenide
Heteroatom-dopant
Density functional theory calculations

ABSTRACT

Hydrogen production from water electrolysis using renewable electricity is a highly promising route to solve the energy crisis of human society. The tetragonal 3d-transition metal selenide with metallic feature has been discovered to efficiently catalyze the hydrogen evolution electrocatalysis; however, its performance is still unsatisfactory and further improvement is necessary. Herein, the hydrogen evolution reaction of the functional tetragonal 3d-transition metal selenide with the heteroatom-dopant as well as cationic vacancy is fully investigated by means of density functional theory calculations. Our results identify 53 promising candidates endowed with good activity due to the absolute free energy of hydrogen adsorption $|\Delta G_H| \leq 0.30$ eV wherein 15 candidates with $|\Delta G_H| \leq 0.09$ eV possess compelling performance in comparison with the benchmark Pt material. Interestingly, the functional CuSe systems account for 29 out of 53 candidates, being high attractive for experimental synthesis. According to the analysis of electronic structure, the enhanced performance stems from the upshift of the sp orbitals, which benefits for the improved affinity toward hydrogen capture. This work provides new direction and guidance for the design of novel electrocatalysts.

To tackle global challenges of the energy crisis and anthropogenic climate change, it is the immediate priority to develop environment-friendly and sustainable alternatives to replace fossil fuels [1–5]. Hydrogen is highly desirable as a clean fuel and has gained great attention owing to its sustainability and high energy density [6–8]. Considering the fact that the free hydrogen is not abundant in nature, a prospective method for the massive production is electrochemical water splitting ($H_2O \rightarrow H_2 + 1/2\ O_2$) [9], which currently catalyzed by the noble metal Pt [10–12]. However, its scarcity and high price hinder the large-scale of its commercial implementation [13–15]. Therefore, the great enthusiasms are focused on the development of the inexpensive and earth-abundant materials with the compelling efficiency for hydrogen evolution reaction (HER) [16–18].

Two-dimensional (2D) materials holding the large reaction area and unique electronic properties are proved to possess great application prospect in the field of electrocatalysis [19–21], such as 2D transition metal selenides [22–25]. In comparison with transition metal sulfides, the strong metallicity and high electrical conductivity of selenium make a majority of transition metal selenides exhibit relative good catalytic performance [26]. Being different from the transition metal selenides with common hexagonal phase, we discovered that a new tetragonal 3d-transition metal selenide (3d-TMSe) delivers the HER activity wherein the performance is limited by the difficulty of the proton capture, which stems from the insufficient adsorption ability [27]. Such 3d-TMSe consisting of the non-noble metal elements are good electronic conductors, which clearly overcome the shortages of noble metals and oxide-based materials [27–30]. Among varied 3d-TMSe, pristine CuSe monolayer provides the best intrinsic basal-plane activity, as reflected by thermodynamic barrier of 0.3 eV [27]. However, it is still unsatisfactory in comparison with the benchmark Pt(111) with thermodynamic barrier of 0.09 eV [31,32]. Therefore, a further activity promotion of tetragonal 3d-TMSe is necessary. To address the question, Zhong *et al.* successfully synthesized the tetragonal CoSe functionalized by Ni dopant and Co vacancy and it exhibits superior activity in acid solution meanwhile the pristine one delivers relative poor performance [29]. The authors demonstrated that the combination of Ni dopant and Co vacancy offers the enhanced adsorption capacity and optimizes the reactivity toward hydrogen production [29]. Since the same difficulty observed among 3d-TMSe, it is reasonable

* Corresponding authors.
E-mail addresses: xiaobb11@mails.jlu.edu.cn (B. Xiao), zhimin.ao@bnu.edu.cn (Z. Ao).

https://doi.org/10.1016/j.cclet.2022.108046
1001-8417/

to conjecture that the strategy of heteroatom-dopant and cationic vacancy will be valid approach to activate the tetragonal 3d-TMSe material [33].

To address our assumption, we systematically investigated the influence of heteroatom substitution and cationic vacancy on the HER activity of 3d-TMSe monolayer by means of density functional theory (DFT) calculations, wherein the 3d/4d transition metal elements are fully considered as the dopants. For simplification, the TM doping 3d-TMSe with and without vacancies are termed as $TM_2@TM_1Se$ and $TM_2@TM_1Se/V_n$, respectively, wherein n stands for the vacancy number. The 3d-TMSe belongs to *P4/nmm* space group and the corresponding atomic structure is the layered stacking along [001] *via* weak van der Waals (vdW) interaction [29,34]. Therefore, we only consider the exposed (001) facet in the following discussion. According to the well-known hydrogen electrode model, the free energy profiles of hydrogen evolution are established and the corresponding promising candidates have been identified wherein 15 candidates with $|\Delta G_H| \leq 0.09$ eV possess compelling performance in comparison with the benchmark Pt material. Furthermore, according to the detail analysis of density of states, the promotional effect is ascribed to the upshifted sp orbitals between basal Se site and hydrogen adsorbate which enhanced the capture ability toward hydrogen adsorption. Herein, our theoretical calculations shed light on designing such experiments in the future.

All calculations were performed within DFT framework as implemented in DMol^3 code [35,36]. The generalized gradient approximation (GGA) with the Perdew-Burke-Ernzerhof functional was utilized to treat the exchange–correlation interaction [37,38]. The DFT Semi-core Pseudopotential (DSPP) core treat method was implemented for relativistic effects of transition metals, which replaces core electrons by a single effective potential and introduces some degree of relativistic corrections into the core [39]. The double numerical atomic orbital augmented by a polarization function (DNP) was chosen as the basis set [35]. A smearing of 0.005 Ha (1 Ha = 27.2114 eV) to the orbital occupation is applied to achieve accurate electronic convergence. In the geometry structural optimization, the convergence tolerances of energy, maximum force and displacement are 1.0×10^{-5} Ha, 0.002 Ha/Å and 0.005 Å, respectively. The spin-unrestricted method was used for all calculations. A conductor-like screening model (COSMO) was used to simulate a H_2O solvent environment [40]. COSMO is a continuum model in which the solute molecule forms a cavity within the dielectric continuum. The DMol^3/COSMO method has been generalized to periodic boundary cases, where the dielectric constant was set as 78.54 for H_2O. The influence of solution correction on the free energy of hydrogen adsorption ΔG_H has been tested and the corresponding data are listed in Table S1 (Supporting information). Wherein, the inclusion of the water environment slightly increases the adsorption ability, in line with the previous reports [27,41]. In order to describe vdW interactions, the Grimme scheme is adopted herein [42]. The $2 \times 2 \times 1$ supercell is an appropriate choice in the consideration of avoiding the interaction among images and reducing the cumbersome calculation. The vacuum region is set to 15 Å in the z direction in the structure of the TMSe monolayer, which is thick enough to avoid the interaction between the periodic layers. For the calculation of transition state (TS) searching, a linear synchronous transit (LST) maximum was first calculated, which was followed by an energy minimization in directions conjugating to the reaction pathway. The TS approximation obtained *via* LST/optimization was then used to perform a quadratic synchronous transit (QST) maximization to find more accurate TSs. The *ab initio* molecular dynamic stimulations (AIMD) were performed at 300 K within the canonical ensemble, that is, constant-temperature, constant-volume ensemble (NVT). The time-scale is 3 ps with the time step of 1 fs.

The energetic feasibility is an important criterion to determine whether materials can be synthesized. Herein, we judged the difficulty of TM_2 cationic substitution from the thermodynamic aspect by means of the formation energy $E_{F(TM2)}$ [43,44], which is calculated as follows:

$$E_{F(TM2)} = E_{TM2-P} - E_P + E_{TM1} - E_{TM2} \quad (1)$$

where $E_{TM2\text{-}P}$ and E_P are the DFT calculated total energies for the TM_1Se monolayer with and without the dopant atoms, respectively. E_{TM1} and E_{TM2} is the chemical potentials for the single TM_1 atom and the dopant TM_2, respectively, in their ground states.

Furthermore, the introduction of TM_1 cationic vacancies in pristine TM_1Se monolayer was considered by the formation energy $E_{F\,(Vn)}$ and evaluated using:

$$E_{F(Vn)} = E_{Vn} - E_P + nE_{TM1} \quad (2)$$

where the symbol n denotes the number of TM_1 element removed from the pristine TM_1Se system to create defects. E_{Vn} is the total energy of the supercell with n vacancies on TM_1Se.

Similarly, the formation energy of the dopant-vacancy complexes $E_{F(TM2-Vn)}$ is calculated using:

$$E_{F(TM2-Vn)} = E_{TM2-Vn} - E_P + E_{TM1} - E_{TM2} + nE_{TM1} \quad (3)$$

where $E_{TM2\text{-}Vn}$ is the total energy of the functional TM_1Se monolayer with the TM_2 dopant and TM_1 vacancies.

Furthermore, the stability of the dopant-vacancy complexes as a bound complex was evaluated by calculating the binding energy E_{Bn}, which is the energy needed to bind/dissociate the defect complex to is constituent species [45]. This can be evaluated as presented in the expression:

$$E_{Bn} = E_{F(TM2-Vn)} - E_{F(Vn)} - E_{F(TM2)} \quad (4)$$

As the well-known descriptor of the hydrogenation process, the free energy of hydrogen adsorption (ΔG_H) is calculated based on the method proposed by Norskov and co-workers [46,47] in which the free energy of $(H^+ + e^-)$ has been substituted by half the chemical potential of a hydrogen molecule. So, the Gibbs free energy change is calculated by the following formula:

$$\Delta G_H = \Delta E_H + \Delta E_{ZPE} - T\Delta S_H \quad (5)$$

where ΔE_{ZPE} is the zero-point energy difference between the adsorbed state and the gas-phase state of hydrogen obtained from vibrational frequency calculation. T denotes the temperature (equal to 298.15 K here). ΔS_H is the entropy difference due to hydrogen adsorption. Herein, pH is assumed as 0 that protons are abundant and accessible for hydrogen production. However, we would like to mention that when the acid electrolyte changes into a non-acid electrolyte, the high kinetic barrier limits the water splitting to supply the proton as revealed by Fig. S1 (Supporting information), which would degrade the HER efficiency [27,48].

The hydrogen adsorption energy ΔE_H is obtained by Eq. 6:

$$\Delta E_H = E_H - E_0 - 1/2E_{H2} \quad (6)$$

where E_H and E_0 are the total energies of the functional TM_1Se with and without hydrogen adsorption, and E_{H2} is the total energy of one free gas-phase H_2 molecule [49], respectively. As a theoretical descriptor of the HER activity, the positive ΔG_H means the difficult hydrogen adsorption, whereas a negative value signifies the low kinetics of hydrogen desorption. Therefore, for a desirable catalyst, the value of ΔG_H should be zero to reach the equilibrium of the hydrogen adsorption strength, that is, neither too strong nor too weak [50,51].

The theoretical overpotential (η) is expressed as the negative value of the absolute free energy of hydrogen adsorption ΔG_H, which is calculated by Eq. 7.

$$\eta = -|\Delta G_H|/e \quad (7)$$

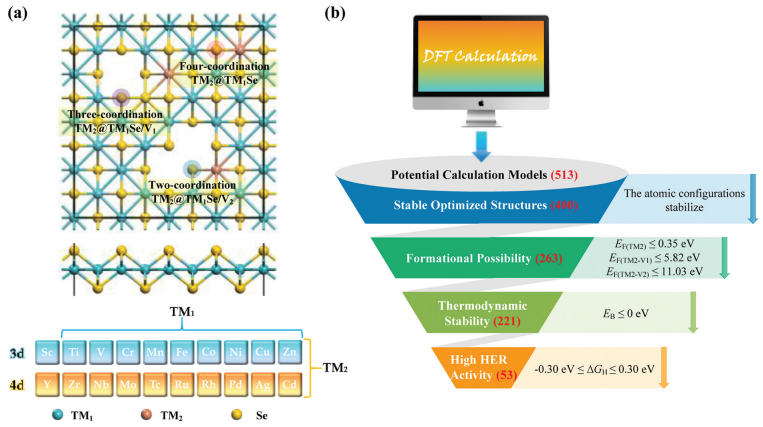

Fig. 1. (a) The atomic structure of $TM_2@TM_1Se$, $TM_2@TM_1Se/V_1$ and $TM_2@TM_1Se/V_2$ models. (b) Workflow of multilevel calculations for seeking thermodynamically stable and catalytically efficient materials.

Fig. 1a schematically presents the theoretical models of $TM_2@TM_1Se$, $TM_2@TM_1Se/V_1$ and $TM_2@TM_1Se/V_2$, wherein $TM_2@TM_1Se$ stands for the TM_1Se monolayer with the TM_2 substitution meanwhile $TM_2@TM_1Se/V_1$ and $TM_2@TM_1Se/V_2$ donate the $TM_2@TM_1Se$ separately decorated by TM_1 single-vacancy and TM_1 double-vacancy pair, that is, they are dopant-vacancy complexes. Considering its feasibility theoretically and experimentally, TM_1 of Ti, V, Cr, Mn, Fe, Co, Ni, Cu and Zn are taken into consideration [27], meanwhile TM_2 are fully screened from 3d/4d TM elements in order to figure out the optimal configurations. Fig. 1b provides the multilevel screening criterion, involving stable lowest-energy structures after geometrical optimization, the energetic feasibility for the experimental synthesis, the thermodynamic stability of dopant-vacancy complexes in order to avoid the separation and the efficiency of hydrogen evaluation featured by the suitable free energy of hydrogen adsorption.

After geometrical optimization, 400 compounds are figured out from a total of 513 initial candidates wherein the configurations with severe structural deformation are discarded. Subsequently, the energetic feasibility of TM_2 substitution as well as the TM_1-vacancy introduction is considered by the formation energy E_F and the corresponding data are listed in Table S2 (Supporting information) wherein the negative values give an indication that the functionalization is exothermic and the positive ones imply that the formation of dopant-vacancy complex needs the extra energy [45,52]. Due to the successful synthesis of Ni@CoSe, $Ni@CoSe/V_1$ and $Ni@CoSe/V_2$ through a simple successive solid-state synthesis and chemical deintercalation method [29], we artificially set their formation energies E_F as the references wherein the corresponding values are 0.35, 5.82 and 11.03 eV, respectively. Fig. 2 reveals that there are 263 compounds energetically preferred, involving 111 in $TM_2@TM_1Se$, 87 in $TM_2@TM_1Se/V_1$ and 65 in $TM_2@TM_1Se/V_2$. Furthermore, the thermodynamic stability of the dopant-vacancy complex as a bound configuration is checked by the binding energy E_B and the corresponding data are listed in Table S3 (Supporting information) wherein the negative values imply the materials will exist as bound complex and do not dissociate into its constituent species, *vice versa* [52–54]. It is noteworthy that the stability mentioned above is argued purely from energetics consideration without taking into account lattice dynamics or other esoteric phenomena such as realistic synthesis conditions. Herein, the screening criterion further narrows the number of dopant-vacancy complexes from 152 to 110, involving 57 in $TM_2@TM_1Se/V_1$ and 53 in $TM_2@TM_1Se/V_2$. In the regard, there are 221 candidates for the activity assessment.

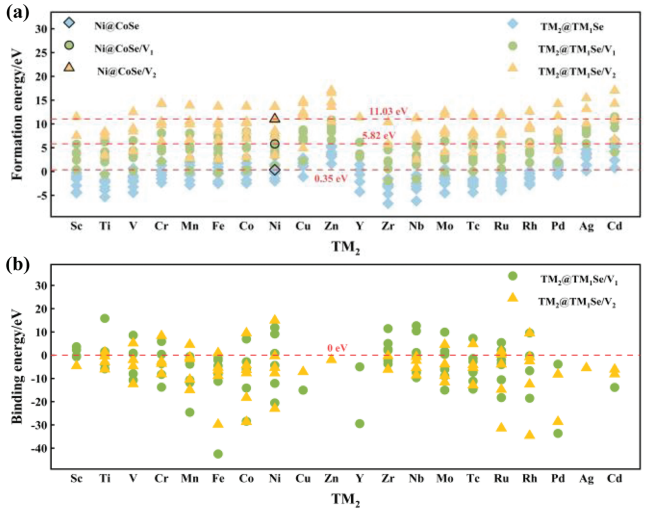

Fig. 2. (a) The formation energies E_F of $TM_2@TM_1Se$, $TM_2@TM_1Se/V_1$ and $TM_2@TM_1Se/V_2$ wherein the E_F of $Ni_2@Co_1Se$, $Ni_2@Co_1Se/V_1$ and $Ni_2@Co_1Se/V_2$ are settled as the references with the corresponding values of 0.35, 5.82 and 11.03 eV, respectively. (b) The binding energies E_B of $TM_2@TM_1Se/V_1$ and $TM_2@TM_1Se/V_2$.

We move on to the assessment of catalytic activity. The adsorption sites are given in Fig. S2 (Supporting information). Although different Se sites offers varied hydrogen affinity, as demonstrated in Tables S4 and S5 (Supporting information), the anion Se in the defective site is considered as adsorbed site for proton capture in our calculations, which is in line with the previous investigation [27,29,55,56]. Despite that reaction mechanism is dependent on the dopant-vacancy combination as shown in Fig. S3 (Supporting information), we adopted the free energy of hydrogen adsorption ΔG_H as our descriptor (the barrier of Volmer step) according to the well-established volcano-relationship between the catalytic activity and ΔG_H. It stems from the Sabatier principle wherein if hydrogen binds too weakly, the formed intermediate will be too low for the reaction to occur and if hydrogen binds too strongly, the product will tend to remain on the surface without desorbing. Therefore, there is an optimum binding energy that maximizes the reaction kinetics [57]. According to the previous works [58,59], the material possessed the absolute ΔG_H within 0.3 eV is widely accepted as good catalyst for hydrogen production. Therefore, we artificially set $-0.30\,eV \leq \Delta G_H \leq 0.30\,eV$ as a criterion window to judge the HER efficiency. The ΔG_H data of 221 candidates are presented in

Table 1
The formation energy E_F, the binding energy E_B, and the free energy of hydrogen adsorption ΔG_H of the screened candidates, involving 5 TM_2@TM_1Se, 16 TM_2@TM_1Se/V_1 and 32 TM_2@TM_1Se/V_2 (E_F, E_B and ΔG_H in eV). The data of pristine CuSe ($\Delta G_H = 0.30$ eV) from Ref. [27].

Type	Model	E_F	E_B	ΔG_H	Type	Model	E_F	E_B	ΔG_H
V_0	CuSe			0.30	V_2	Mn@FeSe/V_2	10.60	−1.55	0.16
	Sc@CuSe	−4.51		0.10		Nb@FeSe/V_2	7.60	−8.57	−0.16
	Ti@CuSe	−5.34		0.30		Mo@FeSe/V_2	8.71	−11.59	0.05
	Y@CuSe	−4.23		0.24		Tc@FeSe/V_2	8.30	−5.39	0.24
	Cu@ZnSe	−1.08		0.28		Ti@CoSe/V_2	0.34	−2.88	0.26
	Ag@ZnSe	0.16		0.19		Nb@CoSe/V_2	7.60	−0.64	0.10
V_1	Y@NiSe/V_1	3.04	−5.01	0.27		Sc@NiSe/V_2	7.52	−4.64	0.00
	Sc@CuSe/V_1	0.42	−0.63	−0.23		Zr@NiSe/V_2	5.71	−6.16	0.11
	Ti@CuSe/V_1	−0.60	−5.89	0.07		Ti@CuSe/V_2	3.40	−6.01	−0.17
	Mn@CuSe/V_1	2.66	−11.78	0.25		V@CuSe/V_2	4.34	−4.69	−0.05
	Fe@CuSe/V_1	2.56	−8.03	0.16		Cr@CuSe/V_2	6.30	−8.06	−0.05
	Co@CuSe/V_1	2.90	−6.25	0.18		Mn@CuSe/V_2	6.71	−10.46	0.00
	Ni@CuSe/V_1	3.31	−4.40	0.10		Fe@CuSe/V_2	6.53	−8.85	−0.11
	Zr@CuSe/V_1	−1.92	−3.79	−0.01		Co@CuSe/V_2	6.90	−6.28	−0.07
	Ru@CuSe/V_1	0.62	−10.55	0.21		Ni@CuSe/V_2	7.28	−5.36	−0.19
	Rh@CuSe/V_1	1.88	−6.71	0.30		Zn@CuSe/V_2	10.52	−1.97	0.14
	Pd@CuSe/V_1	4.58	−3.87	0.20		Nb@CuSe/V_2	2.56	−5.48	−0.03
	Co@ZnSe/V_1	0.34	−28.42	0.23		Mo@CuSe/V_2	4.13	−8.86	−0.10
	Ni@ZnSe/V_1	1.11	−20.53	-0.27		Tc@CuSe/V_2	4.09	−12.89	−0.16
	Cu@ZnSe/V_1	2.22	−15.03	0.21		Ru@CuSe/V_2	4.46	−14.76	−0.13
	Pd@ZnSe/V_1	1.88	−33.63	0.02		Rh@CuSe/V_2	5.68	−12.49	−0.25
	Cd@ZnSe/V_1	4.08	−13.84	0.07		Pd@CuSe/V_2	8.42	−8.24	−0.06
V_2	Co@CrSe/V_2	10.18	−28.62	0.17		Ag@CuSe/V_2	10.11	−5.48	0.26
	Ru@CrSe/V_2	8.30	−31.44	0.24		Cd@CuSe/V_2	11.02	−8.13	0.12
	Rh@CrSe/V_2	9.23	−34.60	0.08		Cu@ZnSe/V_2	4.90	−7.15	0.02
	Fe@MnSe/V_2	8.56	−6.52	0.04		Pd@ZnSe/V_2	4.45	−28.61	0.29
	Ti@FeSe/V_2	8.26	−0.39	0.10		Cd@ZnSe/V_2	6.75	−6.08	−0.10

Table S6 (Supporting information). For clear observation, Table 1 presents the ΔG_H data within ± 0.3 eV including 5 TM_2@TM_1Se, 16 TM_2@TM_1Se/V_1 and 32 TM_2@TM_1Se/V_2 and Fig. 3 provides the free energy profiles of the attractive candidates and the volcano-shaped relation between the theoretical overpotential η and ΔG_H.

In line with the pristine TM_1Se monolayer, the ΔG_H are consistently positive for TM_2@TM_1Se, indicating that the preservation of the weak binding and the difficulty of the proton capture ($H^+ + e^- \rightarrow H^*$) [56]. The data indicate that Sc@CuSe, Ti@CuSe, Y@CuSe, Cu@ZnSe and Ag@ZnSe are within criterion window and the corresponding ΔG_H are 0.10, 0.30, 0.24, 0.28 and 0.19 eV, respectively. In comparison with the pristine CuSe delivered ΔG_H of 0.30 eV, the Sc dopant provides a great activity promotion. Furthermore, the incorporation of Ag with $4d^{10}5s^1$ electron configuration into ZnSe significantly improves the hydrogen production. More interestingly, the combination of heteroatom dopant and cationic vacancy greatly enriches the database of potential candidates. Specifically, there are 4 TM_2@TM_1Se/V_1 and 11 TM_2@TM_1Se/V_2 offered nearly thermo-neutral hydrogen adsorption [31,54], wherein they deliver the comparable or even superior activities in comparison with the benchmark Pt material (ΔG_H = -0.09 eV) [31,32]. For the former, the substitutions of Ti and Zr into CuSe/V_1 as well as Pd and Cd into ZnSe/V_1 deliver ΔG_H of 0.07, -0.01, 0.02 and 0.07 eV, respectively. For the latter, Rh@CrSe/V_2, Fe@MnSe/V_2, Mo@FeSe/V_2, Sc@NiSe/V_2, Cu@ZnSe/V_2 in combination with V, Cr, Mn, Co, Nb and Pd@CuSe/V_2 are highly attractive due to the ΔG_H within ±0.09 eV. Furthermore, Fig. 3d presents the classical volcano curve between the theoretical overpotential η and ΔG_H, clearly confirming the outstanding HER performance of the promising candidates mentioned above. The results provide a visual optimization of 3d-TMSe as hydrogen electrode catalyst *via* introduction of the heteroatom-dopant and cationic vacancy, in line with the previous work [29]. Building on the mentioned discussion, chemical engineering brings colorful combinations to achieve the high activity toward hydrogen production, especially CuSe systems accounted for 29 out of 53 candidates. Fig. 4 summarizes the influence of 3d/4d dopants on the performance of CuSe systems. Wherein, diverse dopant poses different influence on the catalytic activity. Especially, the efficient dopants are separately limited at the elements of Sc, Zn and Y for TM_2@CuSe, and Ti, Ni and Zr for TM_2@CuSe/V_1; however, the abundant choices are presented for TM_2@CuSe/V_2 wherein the optimal element nearly covers 3d/4d dopants.

Due to its structural character, the restacking may be a possible phenomenon for the 2D materials, which would impact the catalytic performance. In our case, introduction of dopant and vacancy into TMSe would not significantly change the interaction between layers as shown in Fig. S4 (Supporting information), as revealed by the corresponding exfoliation energy E_{exf} data listed in Table S7 (Supporting information). The small E_{exf} indicates the easy exfoliation, being in line with the ideal 3d-TMSe layers [27]. Furthermore, it has been demonstrated that the H_2 molecules produced by the electrocatalysis of water splitting will cause layer-exfoliation and suppress layer-agglomeration [27,60]. Therefore, it is reasonable to conjecture that the functional 3d-TMSe could be stay in monolayer state during the work condition.

Besides activity, the life expectancy of catalyst is another profound significance. Therefore, we further evaluated the thermodynamic and electrochemical stabilities of the screened highly-active candidates endowed with ΔG_H within ±0.09 eV. According to the dissolution potential U_{diss} data listed in Table S8 (Supporting information), Zr@CuSe/V_1, Fe@MnSe/V_2, Sc@NiSe/V_2 and Mn@CuSe/V_2 are instable, which would suffer from the TM_2 dissolution under the electrochemical conditions [61]. Furthermore, the thermodynamic stability was further checked in Figs. S5–S7 (Supporting information). According to the corresponding snapshots, severe deformations are observed for Pd@ZnSe/V_1, Cd@ZnSe/V_1 and Cu@ZnSe/V_2 as well as Sc@NiSe/V_2, indicating the structural collapse at the room temperature; meanwhile in despite of the atomic vibration, the preservation of the atomic structures are observed for the rest indicating the thermodynamic stability. Therefore, the stability consideration would further narrow the highly-active candidates. However, the theoretical method adopted herein is not fully addressed the stability issue and the experimental verifica-

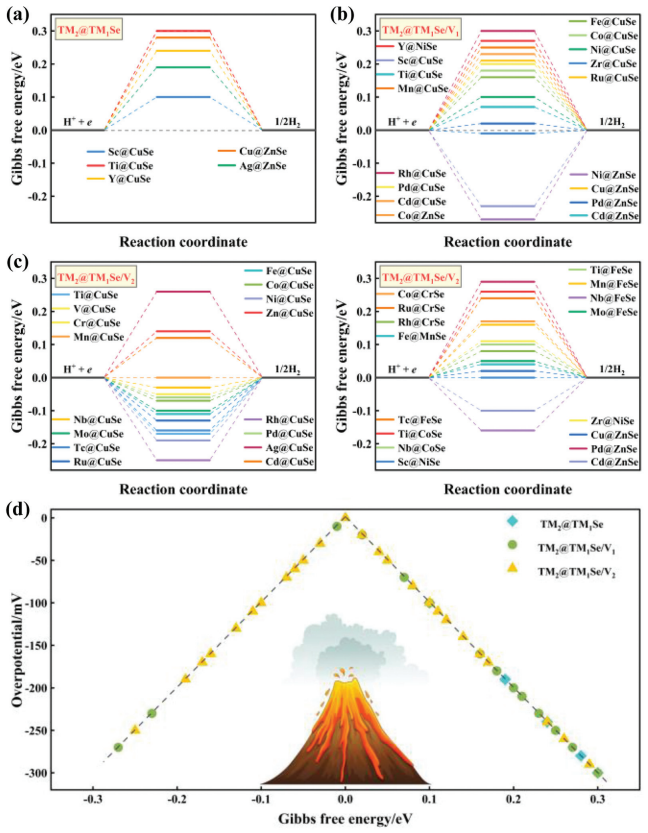

Fig. 3. The free energy diagrams for (a) $TM_2@TM_1Se$, (b) $TM_2@TM_1Se/V_1$ and (c) $TM_2@TM_1Se/V_2$. (d) The volcano curve of the theoretical overpotential η as a function of the free energy of hydrogen adsorption ΔG_H.

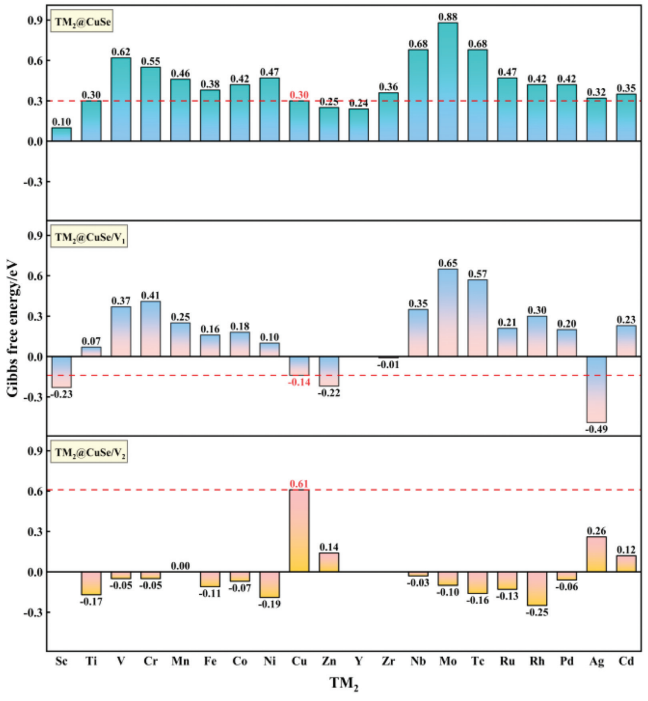

Fig. 4. The free energy of hydrogen adsorption ΔG_H of $TM_2@CuSe$, $TM_2@CuSe/V_1$ and $TM_2@CuSe/V_2$.

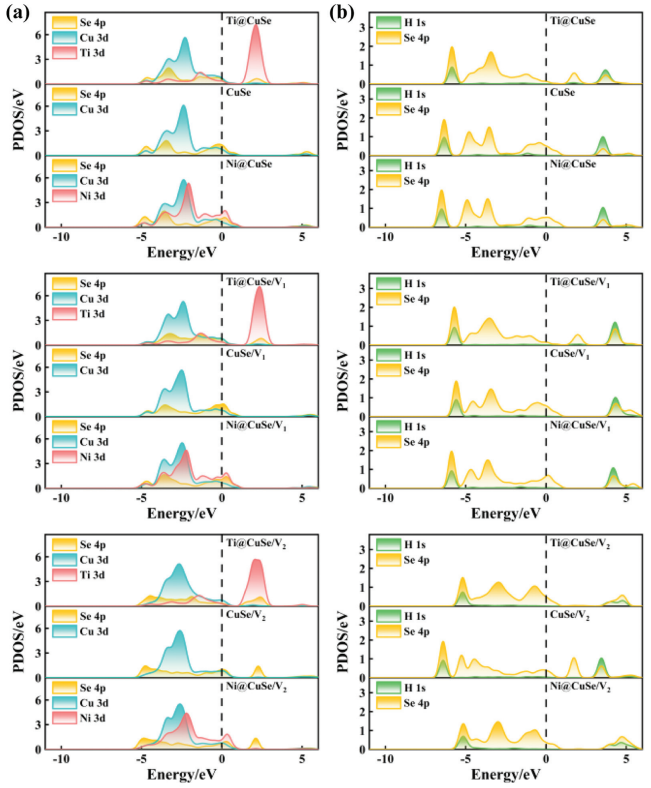

Fig. 5. (a) The partial density of states between Se 4p and its surrounding TM_2/Cu 3d orbitals of $TM_2@CuSe$, $TM_2@CuSe/V_1$ and $TM_2@CuSe/V_2$ without H adsorption (Herein, TM_2 = Ti or Ni). (b) The partial density of states between H 1s and Se 4p orbitals of $TM_2@CuSe$, $TM_2@CuSe/V_1$ and $TM_2@CuSe/V_2$ with H adsorption (Herein, TM_2 = Ti or Ni). The green, yellow, blue and red solid lines represent H 1s, Se 4p, Cu 3d and TM_2 3d orbitals, respectively.

tion is still necessary. Furthermore, since the successful preparation of Ni@CoSe, Ni@CoSe/V_1 and Ni@CoSe/V_2 [29], it seems the synthesis of $TM_2@TMSe/V_1$ and $TM_2@TMSe/V_2$ could be achieved by the similar strategy that introducing the vacancy into alloying $TM_2@TM_1Se$ samples by heating. Therefore, we expect our predicted candidates would be validated in the future.

Considering the interesting variation mentioned above, we focus our attention to figure out the physical origin based on the data of CuSe systems. Herein, Ti and Ni functionalized CuSe, CuSe/V_1 and CuSe/V_2 systems are selected as the illustration to reveal the interaction between Se and its surrounding TM_2/Cu atoms. Fig. 5a demonstrates the orbital couplings between Se 4p and its surrounding TM_2/Cu 3d orbitals. Therein, the orbital coupling between TM_2/Cu d-band and Se p-band leads to different distribution of Se p-band. Therefore, the TM_2/Cu d-orbital is important for the HER process, by means of the tailoring of the Se p-band. With hydrogen attachment on Se site, Fig. 5b presents the partial density of states (PDOS) of $TM_2@CuSe$, $TM_2@CuSe/V_1$ and $TM_2@CuSe/V_2$ (herein TM_2 = Ti or Ni), respectively, exhibiting intensive occurrence of sp-hybridization. For clear observation, the energy levels of sp hybridization below the Fermi level are labeled as p_{max} and the data are given in Table 2. Quantitatively, the p_{max} are −6.50, −6.35 and −5.86 eV for Ni@CuSe, CuSe and Ti@CuSe with the ΔG_H of 0.47, 0.30 and 0.30 eV, respectively. For dopant-vacancy complexes, the p_{max} are −5.88, −5.71 and −5.60 eV for Ni@CuSe/V_1, Ti@CuSe/V_1 and CuSe/V_1 meanwhile −6.41, −5.20, −5.16 eV for CuSe/V_2, Ti@CuSe/V_2 and Ni@CuSe/V_2, respectively, which are in accord with the trend of strengthened adsorption capacity. In despite of some deviation, it seems the parameter of p_{max} provides

Table 2
The free energy of hydrogen adsorption ΔG_H and the sp-hybridization peak p_{max} of the functional CuSe systems, involving 3 TM_2@CuSe, 10 TM_2@CuSe/V_1 and 16 TM_2@CuSe/V_2 (ΔG_H and p_{max} in eV). The data of pristine CuSe ($\Delta G_H = 0.30$ eV, $p_{max} = -6.35$ eV) from Ref. [27].

Type	Model	ΔG_H	p_{max}	Type	Model	ΔG_H	p_{max}
V_0	CuSe	0.30	−6.35	V_2	Ti@CuSe/V_2	−0.17	−5.20
	Sc@CuSe	0.10	−5.45		V@CuSe/V_2	−0.05	−5.23
	Ti@CuSe	0.30	−5.86		Cr@CuSe/V_2	−0.05	−5.33
	Y@CuSe	0.24	−5.63		Mn@CuSe/V_2	0.00	−5.36
V_1	CuSe/V_1	−0.14	−5.60		Fe@CuSe/V_2	−0.11	−5.19
	Sc@CuSe/V_1	−0.23	−5.39		Co@CuSe/V_2	−0.07	−5.19
	Ti@CuSe/V_1	0.07	−5.71		Ni@CuSe/V_2	−0.19	−5.16
	Mn@CuSe/V_1	0.25	−6.07		Zn@CuSe/V_2	0.14	−5.53
	Fe@CuSe/V_1	0.16	−5.99		Nb@CuSe/V_2	−0.03	−5.27
	Co@CuSe/V_1	0.18	−6.01		Mo@CuSe/V_2	−0.10	−5.29
	Ni@CuSe/V_1	0.10	−5.88		Tc@CuSe/V_2	−0.16	−5.22
	Zr@CuSe/V_1	−0.01	−5.61		Ru@CuSe/V_2	−0.13	−5.32
	Ru@CuSe/V_1	0.21	−6.14		Rh@CuSe/V_2	−0.25	−4.98
	Rh@CuSe/V_1	0.30	−6.01		Pd@CuSe/V_2	−0.06	−5.52
	Pd@CuSe/V_1	0.20	−5.71		Ag@CuSe/V_2	0.26	−5.87
V_2	CuSe/V_2	0.61	−6.41		Cd@CuSe/V_2	0.12	−5.62

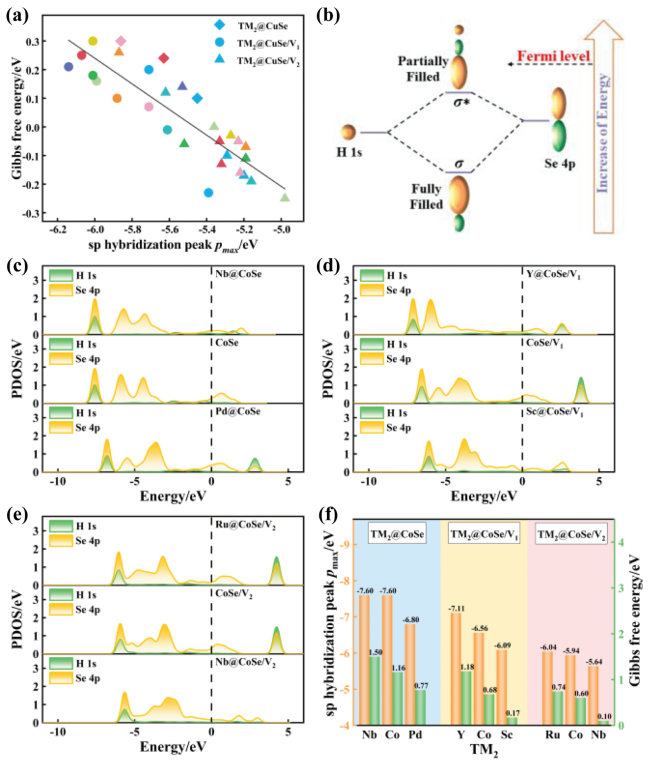

Fig. 6. (a) The fitting between the free energy of hydrogen adsorption ΔG_H and the energy level of sp hybridization peak p_{max} of the functional CuSe systems. (b) The schematic diagram of the sp interaction. (c) The partial density of states between H 1s and Se 4p orbitals of Nb@CoSe, CoSe and Pd@CoSe. (d) The partial density of states between H 1s and Se 4p orbitals of Y@CoSe/V_1, CoSe/V_1 and Sc@CoSe/V_1. (e) The partial density of states between H 1s and Se 4p orbitals of Ru@CoSe/V_2, CoSe/V_2 and Nb@CoSe/V_2. (f) The summary of ΔG_H and p_{max} of the functional CoSe systems.

an electron descriptor for the ΔG_H variation wherein the upshifted p_{max} results in the enhanced affinity toward hydrogen.

To confirm our conjecture, Fig. 6a presents the linear relationship between the ΔG_H and p_{max} for the functional CuSe systems, clearly supporting the intrinsic dependence of ΔG_H on p_{max}. The p-band center theory provides a theoretical explanation [62,63]. As illustrated in Fig. 6b, the sp interaction leads to the formation of the anti-bonding state σ^* that normally goes across the Fermi level and the bonding orbital σ that is positioned under the Fermi level [64,65]. The sp hybridization peak stands for the location of fully filling bonding orbital σ. That is, with a higher location of the hybridization peak, the anti-bonding states move higher with a lower occupancy, leading to the stronger ΔG_H [66]. To further confirm the p-band center theory, Fig. S8 (Supporting information) describes the fitting between Se p-band center ε_p and ΔG_H. The similar linear relation is observed which demonstrates that the Se with higher ε_p offers the stronger ΔG_H, in line with the classical p-band theory. The tendency is consistent with the scaling relation between the p_{max} and the ΔG_H. Before ending our discussion, we extend our analysis on the CoSe systems due to its experimental success [29], in order to verify the universality of the p_{max}. Herein, the functional CoSe systems featured with the maximum and minimum binding strengths are demonstrated as an illustration. The PDOS given in Figs. 6c–e consistently reveal the strong orbital couplings between H 1s and Se 4p orbitals, confirming the formation of H-Se bond, which is identical phenomenon observed in the functional CuSe systems. Fig. 6f summarizes the p_{max} and ΔG_H of the functional CoSe systems discussed above and reveals that the upshifted p_{max} enhances the hydrogen adsorption. The results clearly support the dominant role played by the Se p-band. As a short summary, the improved affinity stems from the upshift of the sp orbitals.

In summary, the HER activities of the tetragonal 3d-TMSe functionalized by heteroatom dopant and Co cationic vacancy are systematically investigated by the density functional theory calculations. Through the lens of thermodynamic stability and free energy profiles, we screened out 5 TM_2@TM_1Se, 16 TM_2@TM_1Se/V_1 and 32 TM_2@TM_1Se/V_2 endowed with high HER activities. It is noteworthy that CuSe systems accounted for 29 out of 53 candidates. Herein, the dopant-vacancy strategy contributes to upshift p orbital and activate the basal Se site, which significantly leads to the strengthened H affinity and thereby the improved catalytic activity. The results provide a clear guidance for the design of novel electrocatalysts for hydrogen evolution.

Declaration of competing interest

The authors declare that they have no known competing financial interests or personal relationships that could have appeared to influence the work reported in this paper.

Acknowledgments

We acknowledge the supports from the National Natural Science Foundation of China (Nos. 21503097, 51631004, 51701152, 21806023, and 51702345) and Natural Science Foundation of Shaanxi Province (No. 2018JQ5181).

References

[1] J. Luo, J.H. Im, M.T. Mayer, et al., Science 345 (2014) 1593–1596.
[2] W. Zhong, B. Xiao, Z. Lin, Z. Wang, L. Gu, Adv. Mater. 33 (2021) 2007894.
[3] H. Yuan, L. Kong, T. Li, Q. Zhang, Chin. Chem. Lett. 28 (2017) 2180–2194.
[4] C.M. Li, D.Q. Zhu, S.S. Cheng, et al., Chin. Chem. Lett. 33 (2022) 1141–1153.
[5] Z.L. Xu, Z.M. Ao, M. Yang, S.B. Wang, J. Hazard. Mater. 424 (2022) 127427.
[6] L.X. Lin, P. Sherrell, Y.Q. Liu, et al., Adv. Energy Mater. 10 (2020) 1903870.
[7] Y.Q. Deng, L.J.Y ang, Y.K. Wang, et al., Chin. Chem. Lett. 32 (2021) 511–515.
[8] C. Cui, R.F. Cheng, C. Zhang, X.H. Wang, Chin. Chem. Lett. 31 (2020) 988–991.
[9] J.Q. Zhang, X. Shang, H. Ren, et al., Adv. Mater. 31 (2019) 1905107.
[10] X.Y. Wang, Y. Fei, W. Wang, W.Y.Y Uan, C.M. Li, ACS Appl. Energy Mater. 2 (2019) 8851–8861.
[11] D. Zhou, B. Jiang, R. Yang, X.D. Hou, C.B. Zheng, Chin. Chem. Lett. 31 (2020) 1540–1544.
[12] Y.Q. Ji, J.Q. Xie, Y. Yang, et al., Chin. Chem. Lett. 31 (2020) 855–858.
[13] J.Q. Zhang, Y.F. Zhao, X. Guo, et al., Nat. Catal. 1 (2018) 985–992.
[14] X. Luo, P.X. Ji, P.Y. Wang, et al., Adv. Energy Mater. 10 (2020) 1903891.
[15] J.Q. Li, M.T. Li, H.Q. Sun, et al., ACS Catal. 10 (2020) 3516–3525.
[16] Y.X. Wang, H.Y. Su, Y.H. He, et al., Chem. Rev. 120 (2020) 12217–12314.
[17] Q. Li, Y.C. Wang, J. Zeng, et al., Chin. Chem. Lett. 32 (2021) 3355–3358.
[18] K.D. Xia, J.P. Guo, C.J. Xuan, et al., Chin. Chem. Lett. 30 (2019) 192–196.

[19] D.D. Wang, Y.Q. Zou, L. Tao, et al., Chin. Chem. Lett. 30 (2019) 826–838.
[20] T. Guo, L.N. Wang, S. Sun, et al., Chin. Chem. Lett. 30 (2019) 1253–1260.
[21] G.L. Liu, J.H. Zhou, W.N. Zhao, Z.M. Ao, T.C. An, Chin. Chem. Lett. 31 (2020) 1966–1969.
[22] K. Xu, H. Ding, H.F. Lv, et al., ACS Catal. 7 (2017) 310–315.
[23] H.H. Lin, Q. Zhu, D.H. Shu, et al., Nat. Mater. 18 (2019) 602–607.
[24] X.Y. Xia, L.J. Wang, N. Sui, V.L. Colvin, W.W. Yu, Nanoscale 12 (2020) 12249–12262.
[25] Y. Chang, P.L. Zhai, J.G. Hou, J.J. Zhao, J.F. Gao, Adv. Energy Mater. 12 (2022) 2102359.
[26] H.T. Wang, D.S. Kong, P. Johanes, et al., Nano Lett. 13 (2013) 3426–3433.
[27] B.B. Xiao, Q.Y. Huang, J. Wu, E.H. Song, Q. Jiang, Appl. Surf. Sci. 591 (2022) 153249.
[28] J.K. Noerskov, T. Bligaard, A. Logadottir, et al., J. Electrochem. Soc. 36 (2005) e12154.
[29] W.W. Zhong, Z.P. Wang, N. Gao, et al., Angew. Chem. Int. Ed. 59 (2020) 22743–22748.
[30] Y.L. Zhu, Q. Lin, Y.J. Zhong, et al., Energy Environ. Sci. 13 (2020) 3361–3392.
[31] N. Ran, B. Sun, W.J. Qiu, et al., J. Phys. Chem. Lett. 12 (2021) 2102–2111.
[32] P. Sen, K. Alam, T. Das, R. Banerjee, S. Chakraborty, J. Phys. Chem. Lett. 11 (2020) 3192–3197.
[33] S.Y. Lan, B.H. Jing, C. Yu, et al., Small 18 (2022) 2105279.
[34] Z.P. Lin, C.W. Wang, Z.P. Wang, et al., Electrochim. Acta 294 (2019) 142–147.
[35] B. Delley, J. Chem. Phys. 92 (1990) 508–517.
[36] B. Delley, Comp. Mater. Sci. 17 (2000) 122–126.
[37] J.P. Perdew, K. Burke, M. Ernzerhof, Phys. Rev. Lett. 77 (1996) 3865–3868.
[38] Z.H. Dai, D.D. Li, Z.M. Ao, S.B. Wang, T.C. An, J. Hazard. Mater. 405 (2021) 124684.
[39] B. Delley, Phys. Rev. B 66 (2002) 155125.
[40] T.T. Todorova, B. Delley, Mol. Simulat. 34 (2008) 1013–1017.
[41] B.B. Xiao, Z. Zhang, L.B. Yu, et al., Surf. Interfaces 33 (2022) 102232.
[42] B.B. Xiao, X.Y. Lang, Q. Jiang, RSC Adv. 4 (2014) 28400–28408.
[43] K.O. Obodo, L.L. Noto, S.J. Mofokeng, et al., Mater. Res. Express 5 (2018) 106202.
[44] K.O. Obodo, G. Gebreyesus, C. Ouma, RSC Adv. 10 (2020) 15670–15676.
[45] C.N.M. Ouma, K.O. Obodo, M. Braun, G.O. Amolo, D. Bessarabov, Appl. Surf. Sci. 470 (2019) 107–113.
[46] A.V. Aldes, Z.W. Qu, G.J. Kroes, J. Rossmeisl, J.K. Norskov, J. Phys. Chem. C 112 (2008) 9872–9879.
[47] J. Rossmeisl, Z.W. Qu, H. Zhu, G.J. Kroes, J.K. Norskov, J. Electroanal. Chem. 607 (2007) 83–89.
[48] X.N. Zheng, Y. Yao, W. Ye, P. Gao, Y. Liu, Chem. Eng. J. 413 (2021) 128027.
[49] T.W. He, C.M. Zhang, A.J. Du, Chem. Eng. Sci. 194 (2019) 58–63.
[50] S.S. Ding, P. He, W.R. Feng, et al., J. Phys. Chem. Solids. 91 (2016) 41–47.
[51] L.S. Peng, X.Q. Zheng, L. Li, et al., Appl. Catal. B: Environ. 245 (2019) 122–129.
[52] I.C. Onyia, S.O. Ezeonu, D. Bessarabov, K.O. Obodo, Comp. Mater. Sci. 197 (2021) 110613.
[53] B.B. Xiao, L. Yang, H.Y. Liu, X.B. Jiang, Q. Jiang, Appl. Surf. Sci. 537 (2021) 147846.
[54] Y.J. Yang, J. Liu, F. Liu, Z. Wang, D.J. Wu, J. Mater. Chem. A 9 (2021) 2438–2447.
[55] D. Putungan, S.H. Lin, J.L. Kuo, Phys. Chem. Chem. Phys. 17 (2015) 21702–21708.
[56] Q. Tang, D.E. Jiang, ACS Catal. 6 (2016) 4953–4961.
[57] J. Greeley, T.F. Jaramillo, J. Bonde, I.B. Chorkendorff, J.K. Norskov, Nat. Mater. 5 (2006) 909–913.
[58] C. Tsai, K.R. Chan, J.K. Norskov, F. Abild-Pedersen, Catal. Sci. Technol. 5 (2015) 246–253.
[59] Q. Wang, Z.L. Zhao, S. Dong, et al., Nano Energy 53 (2018) 458–467.
[60] Y.Y. Liu, J.J. Wu, K.P. Hackenberg, et al., Nat. Energy 2 (2017) 17127.
[61] X. Guo, S. Lin, J. Gu, et al., ACS Catal. 9 (2019) 11042–11054.
[62] Y. Jiao, Y. Zheng, M. Jaroniec, S.Z. Qiao, J. Am. Chem. Soc. 136 (2014) 4394–4403.
[63] Y. Jiao, Y. Zheng, K. Davey, S.Z. Qiao, Nat. Energy 1 (2016) 16130.
[64] C. Ling, S. Li, Y. Ouyang, C. Qian, J. Wang, Adv. Sci. 3 (2016) 1600180.
[65] Y.W. Cheng, J.H. Dai, Y.M. Zhang, Y. Song, J. Mater. Chem. A 6 (2018) 20956–20965.
[66] J. Zheng, X. Sun, J. Hu, et al., ACS Appl. Mater. Interfaces 13 (2021) 50878–50891.